Supporting Information

for

The role of gas flow distributions on CO_2 mineralization within monolithic cemented composites: Coupled CFD-factorial design approach

Iman Mehdipour ([,†]), Gabriel Falzone ([*,†]), Dale Prentice ([*,†]), Narayanan Neithalath ([‡]), Dante Simonetti ([†,§]), Gaurav Sant ([*,†,**,††,&])*

[*] Laboratory for the Chemistry of Construction Materials (LC^2), Department of Civil and Environmental Engineering, University of California, Los Angeles, CA 90095, USA

[†] Institute for Carbon Management (ICM), University of California, Los Angeles, CA 90095, USA

[‡] School of Sustainable Engineering and the Built Environment, Arizona State University, Tempe, AZ 85287, USA

[§] Department of Chemical and Biomolecular Engineering, University of California, Los Angeles, CA 90095, USA

[**] Department of Materials Science and Engineering, University of California, Los Angeles, CA 90095, USA

[††] California Nanosystems Institute (CNSI), University of California, Los Angeles, CA 90095, USA

[&] Corresponding author: G. Sant, Phone: (310) 206-3084, Email: gsant@ucla.edu

Number of pages: 8 (including the title page)
Number of figures: 7
Number of tables: 3

(A) Oxide composition of binders

The bulk oxide composition of the fly ash and ordinary portland cement (OPC) is presented in Table S1. The median particle size diameters (d_{50}) of the portlandite, fly ash, and OPC were determined as 3.8 µm, 8.9 µm, and 17.2 µm, respectively, using static light scattering (SLS; LS13-320, Beckman Coulter). Their densities were measured as 2340 kg/m^3, 2440 kg/m^3, and 3140 kg/m^3, respectively, using helium pycnometry (Accupyc II 1340, Micromeritics).

Table S1: Oxide composition (by mass) of the fly ash and OPC as determined by X-ray fluorescence (XRF).

Oxide	Mass (%)	
	Fly ash	OPC
SiO_2	51.60	20.60
Al_2O_3	21.65	4.64
Fe_2O_3	16.81	2.80
SO_3	0.50	2.93
CaO	2.18	64.28
Na_2O	0.82	0.18
MgO	0.78	2.03
K_2O	2.29	0.32

(B) Concrete block forming process

Figure S1 presents photographs of the block-making machine (Stonemaker DM100) that was used to produce standard concrete masonry units (CMUs) herein.

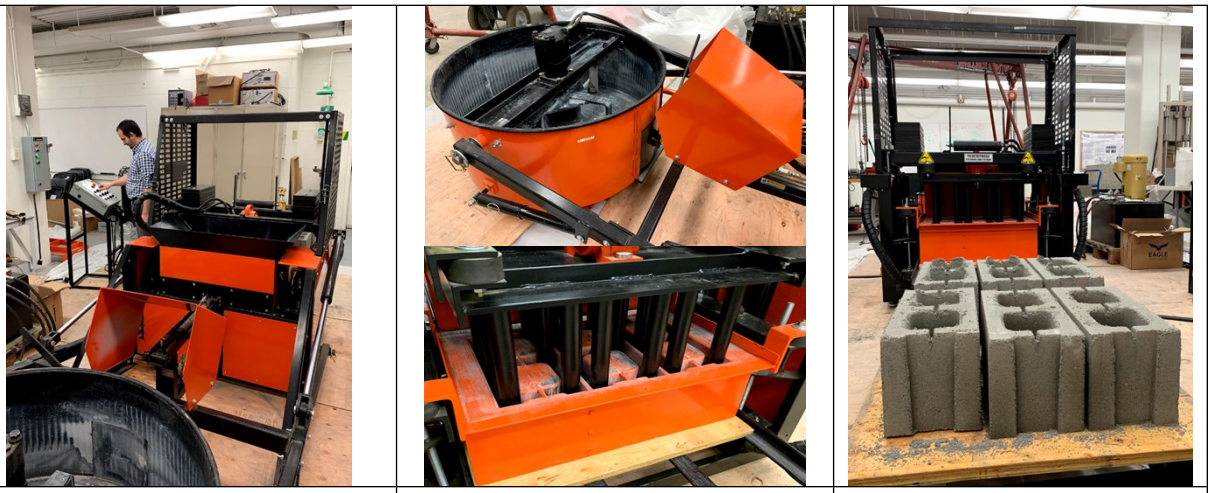

(a) **(b)** **(c)**

Figure S1: Photographs of the block-making machine system used for the production of prototype concrete masonry units, including **(a)** a view of the block-making machine and control panel, **(b)** a view of the pan-style mixer and mold press setup, and **(c)** a view of the product offload track after extracting freshly produced concrete masonry units.

The machine performs mixing, material loading, and block forming actions – via hydraulic actuation – and is controlled by a digital control panel (Figure S1a). Fresh mixtures (containing the binder, aggregate, and water) are batched and homogenized in a pan mixer (Figure S1b). The mixing container is raised hydraulically to drop the homogenized concrete mixture into a hopper. The hopper then feeds the material into the block mold (Figure S1b), which forms three CMUs simultaneously. The top section of the mold compacts the materials into a block shape by hydraulic compaction and vibration. The formed blocks – i.e., fresh masonry units, or "green bodies" – are loaded on plywood pallets and ejected on a track for off-loading (Figure S1c).

(C) Factorial Design-of-Experiments

Table S2 presents the factorial Design-of-Experiments (DoE) that was used to assess the effects of gas processing parameters (*T*, *RH*, and *Q*) on the carbonation of concrete blocks. Factorial DoE consists of three different parts: (i) factorial part (2^n, n: number of design variables), (ii) central part, and (iii) validation part within the design space. The significance of variables and their interactions are determined by the analysis of variance (ANOVA) using the least-squares fitting. In this study, the probability (P-values) less than 0.05 was considered as a level of significance.[1] For this series of experiments, the concrete blocks were first dried under exposure to flowing air to achieve different initial S_w prior to the carbonation process.

Table S2: Factorial Design-of-Experiments to assess the effects of gas processing parameters on carbonation of concrete block. The upper and lower bounds for each design variable are indicated. The top flow configuration was applied to all cases.

Type	Mixture ID	Coded value			Absolute value		
		T	*RH*	*Q*	*T* (°C)	*RH* (%)	*Q* (slpm)
Factorial points	1	-1.0	-1.0	-1.0	20	20	0.10
	2	-1.0	-1.0	1.0	20	20	4.92
	3	-1.0	1.0	-1.0	20	60	0.10
	4	1.0	-1.0	-1.0	50	20	0.10
	5	-1.0	1.0	1.0	20	60	4.92
	6	1.0	-1.0	1.0	50	20	4.92
	7	1.0	1.0	-1.0	50	60	0.10
	8	1.0	1.0	1.0	50	60	4.92
Central points for 3 replicates	9	0.0	0.0	0.0	35	40	2.51
Validation points	10	0.33	0.50	-0.21	40	50	2.0
	11	1.0	-1.0	-0.50	50	20	1.30
	12	0.0	-1.0	0.20	35	20	3.0
	13	1.0	0.0	0.41	50	40	3.50

(D) Sampling procedure for CO_2 uptake characterization

Figure S2 depicts the powder sampling procedure for each block section (i.e., 2 sides, 2 faces, and web) to assess the variation of CO_2 uptake across different concrete block sections.

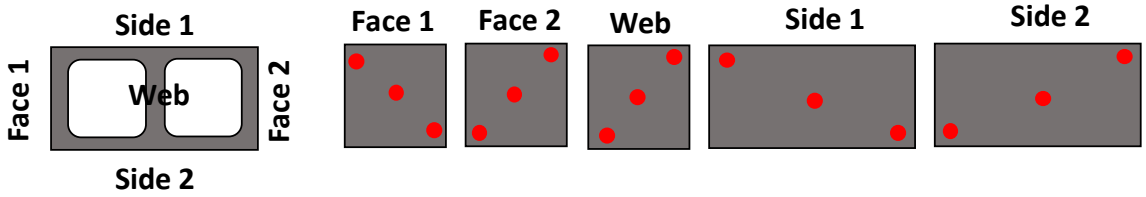

Figure S2: A schematic depicting powder sampling procedure for assessing CO_2 uptake of carbonated concrete block. Each concrete block was sampled from five different sections (i.e., 2 sides, 2 faces, and web). The powder samples that are extracted at different locations are indicated as red points.

(E) CFD and FEM governing equations

CFD modeling: In the $k-\omega$ model, the turbulent kinetic energy k and specific turbulent dissipation rate ω describe turbulence flow. The equations governing the k and ω are given by[2]:

$$\frac{\partial}{\partial t}(\rho k)+\frac{\partial}{\partial x_j}(\rho u_j k)=\rho\tau_{ij}\frac{\partial u_i}{\partial x_j}-\beta^*\rho k\omega+\frac{\partial}{\partial x_j}\left[\left(\mu+\sigma^*\frac{\rho k}{\omega}\right)\frac{\partial k}{\partial x_j}\right] \quad \textbf{[Eq. S1]}$$

$$\frac{\partial}{\partial t}(\rho \omega)+\frac{\partial}{\partial x_j}(\rho u_j \omega)=\alpha\frac{\omega}{k}\rho\tau_{ij}\frac{\partial u_i}{\partial x_j}-\beta\rho\omega^2+\sigma_d\frac{\rho}{\omega}\frac{\partial k}{\partial x_j}\frac{\partial \omega}{\partial x_j}+\frac{\partial}{\partial x_j}\left[\left(\mu+\sigma\frac{\rho k}{\omega}\right)\frac{\partial \omega}{\partial x_j}\right] \quad \textbf{[Eq. S2]}$$

where ρ is the mean mass density, x_j is the position vector, u_j is the velocity vector, μ is the eddy viscosity, and τ_{ij} is the Reynolds-stress tensor. σ^* and β^* are closure coefficients in the turbulence-kinetic energy equation. The k and ω can be approximated by[2]:

$$k=\frac{3}{2}(uI_T)^2 \quad \textbf{[Eq. S3]}$$

$$\omega=\frac{\sqrt{k}}{(\beta_0^*)^{1/4}L_T} \quad \textbf{[Eq. S4]}$$

where I_T and L_T are turbulent intensity and turbulent length scale, respectively, which are estimated as[2–4]:

$$I_T=0.16(Re)^{-1/8} \quad \textbf{[Eq. S5]}$$

$$L_T=0.07d_{inlet} \quad \textbf{[Eq. S6]}$$

where d_{inlet} is the gas inlet diameter. The I_T and L_T were calculated as 0.05 and 0.00043 m, respectively, and the parameter β_0^* was taken as 0.09.[2]

FEM simulation: The linear elastic boundary value problem in each component of the composite material is defined by the (i) differential equilibrium equations, (ii) the strain-displacement relationships, and (iii) the constitutive relations. First, in the absence of body forces, the differential equilibrium equation in any component is expressed as[5]:

$$\nabla.\sigma=0 \quad \textbf{[Eq. S7]}$$

Second, the strain–displacement relation in any component is given by:

$$\epsilon=\frac{1}{2}[\nabla u+\nabla^T u] \quad \textbf{[Eq. S8]}$$

where $u = [u,v,w]^T$ is the displacement vector. Finally, the linear elastic constitutive relation is given by:

$$\sigma = C : \epsilon \qquad \textbf{[Eq. S9]}$$

where σ and ϵ are the stress and strain tensors, respectively, and C is the fourth-order stiffness tensor. The latter is a property of the material and depends on its microstructure and temperature. For homogeneous and isotropic materials, the sensor C is given by:

$$C_{ijkl} = \lambda\delta_{ij}\delta_{kl} + \mu(\delta_{ik}\delta_{jl} + \delta_{il}\delta_{jk}) \qquad \textbf{[Eq. S10]}$$

where λ and μ are the Lamé parameters, and $\delta_{\alpha\beta}$ denotes a Kronecker delta. The material tensor in Eq. (S10) can also be expressed in terms of elastic moduli, using the following identities:

$$\lambda = \frac{E\nu}{(1+\nu)(1-2\nu)} = K - \frac{2}{3}G \quad \text{and} \quad \mu = \frac{E}{2(1+\nu)} = G \qquad \textbf{[Eq. S11]}$$

where E, K, and G are the Young's, bulk, and shear moduli, respectively, and ν is the Poisson's ratio. Combining Eqs. (S7)–(S9) results in governing equations expressed solely in terms of the displacement field. These equations are referred to as Navier's equations that are given by:

$$(\lambda_l + \mu_l)\nabla(\nabla . u_l) + \mu_l\nabla^2 u_l = 0 \qquad \textbf{[Eq. S12]}$$

(F) CO_2 uptake variations

Figure S3(a) shows the variations of CO_2 uptake for the different concrete block's sections for different gas flow configurations. Top flow provided the most uniform carbonation. The strong dependence of carbonation rate constant on drying rate constant is indicated in Figure S3(b).

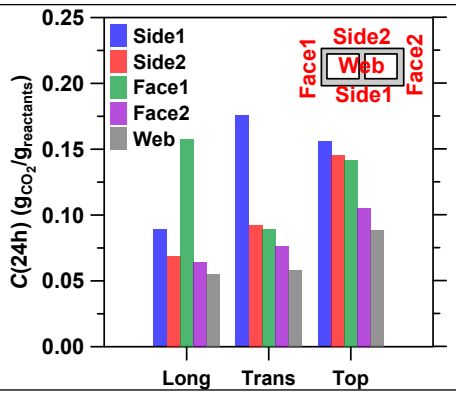

(a)

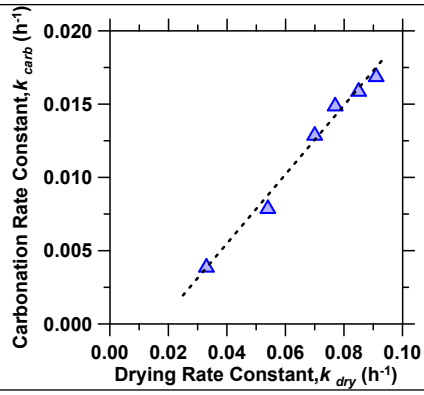

(b)

Figure S3: (a) The variations in the 24-h CO_2 uptake of different sections of the concrete block under different gas flow configurations. **(b)** The dependence of carbonation rate constant on drying rate constant. In all carbonation experiments, gas stream featured [CO_2] = 12.5 % at *T* = 70 °C, *RH* = 50 %, and 2.45 slpm flow rate. In drying experiments, the air stream featured [CO_2] = 0.04 %, *T* = 70 °C, *RH* = 50 %, and 2.45 slpm flow rate.

(G) CFD simulations of contacting gas velocity

The variations in contacting gas velocity across the concrete block's surfaces are indicated in Figure S4(a). Increasing contacting gas velocity resulted in a higher reduction of pore water

saturation S_w (Figure S4b). The effect of contacting gas velocity on CO_2 uptake for different sections of concrete block is displayed in Figure S4(c).

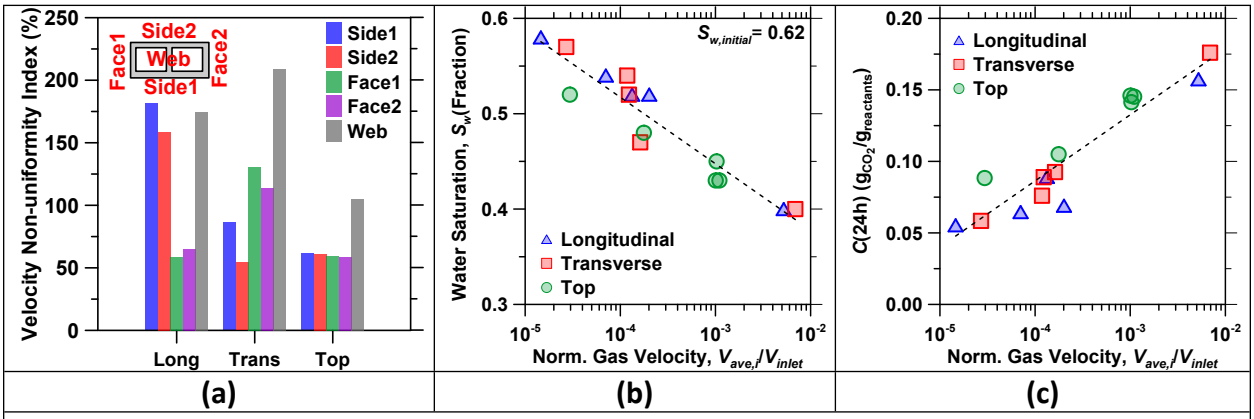

Figure S4: (a) The CFD analysis of velocity non-uniformity index across different surfaces of the concrete block for varying gas flow configurations. **(b)** The variations of pore water saturation S_w across different concrete block's sections as a function of contacting gas velocity. Concrete block featured $S_{w,initial} = 0.62$ prior to the onset of the carbonation process. **(c)** The effect of contacting gas velocity across surfaces of concrete block on 24-h CO_2 uptake. In all cases, gas stream featured [CO_2] = 12.5 % at *T* = 70 °C, *RH* = 50 %, and 2.45 slpm flow rate.

(H) Derivation of statistical prediction models

Table S3 presents the ANOVA results and derived statistical prediction models for pore water saturation and CO_2 uptake.

Table S3: Analysis of variance (ANOVA) results of factorial design used for carbonation performance evaluation of concrete block.

Response	Parameter	F value	p-value Prob > F	Contribution (Actual factor)	R^2	R^2_{adj}
$S_{w,drying}$ (after drying and prior to carbonation)	Model	13.20	0.0072		0.92	0.85
	Constant			0.62890		
	T	9.18	0.0291	-0.00397		
	RH	23.62	0.0046	0.00198		
	Q	12.54	0.0165	-0.07348		
	*T*RH*		NS			
	*T*Q*		NS			
	*RH*Q*	7.46	0.0412	0.00111		
	Curvature	1.97	0.2195			
C(24h)	Model	16.48	0.0044		0.93	0.87
	Constant			-0.00592		
	T	5.23	0.0709	0.00127		
	RH	19.38	0.0070	-0.00022		
	Q	27.48	0.0033	0.04373		

*T*RH*		NS	
*T*Q*		NS	
*RH*Q*	13.85	0.0137	-0.00064
Curvature	7.95	0.0371	

Notes: *T*: gas temperature. *RH*: gas relative humidity. *Q*: gas flow rate. NS: not significant. Values of "Prob > F" less than 0.05 indicate that model terms are significant. The "Prob > F" determines if the curvature of response is significant as measured by the difference between the average of the central points and the average of the factorial points in the design space.

Figure S5 compares the accuracy of the derived statistical prediction model for the 24-h CO_2 uptake response for four additional gas processing conditions within the design space. The two diagonal dashed lines represent 95 % confidence interval bounds. The predicted data points lie reasonably close to the 1:1 diagonal line, confirming the validity of the prediction model.

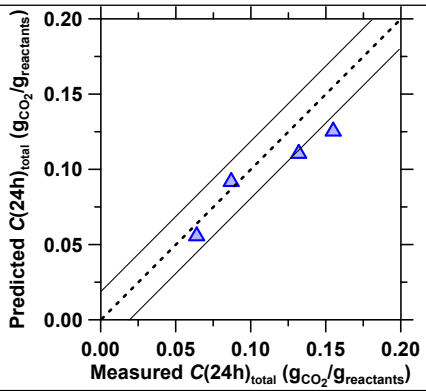

Figure S5: Comparison between measured and predicted 24-h CO_2 uptake response. Four additional gas processing conditions were randomly selected within the design domain (see Table S2) to validate the accuracy of the derived statistical models. The two diagonal solid lines represent 95 % confidence interval bounds.

(I) Desirability response for multivariable optimization

Figure S6 displays an example of the desirability response surface of gas processing conditions to meet the performance targets. The targets were defined as maximizing the overall CO_2 uptake and minimizing the non-uniformity of CO_2 uptake across different block's sections. Increasing gas flow rate and decreasing gas *RH* results in enhanced desirability response so long as the pore water saturation of concrete block exceeds the critical value; $S_w > S_{w,c} \approx 0.10$.

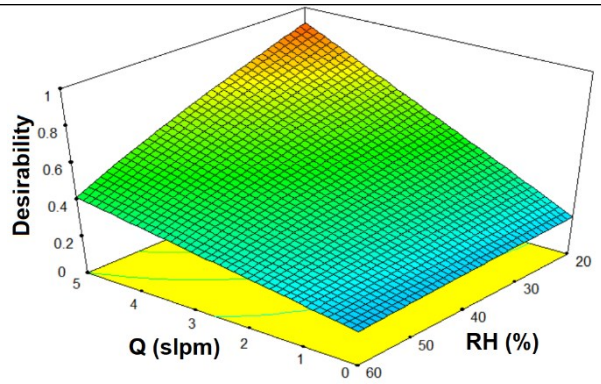

Figure S6: Desirability surface response of gas processing conditions to satisfy the defined performance targets. The desirability value close to 1 determines the optimal combination of variables that satisfies the target properties.

(J) FEM analysis of the uniaxial compressive response of concrete block

The FEM simulations of stress-displacement responses of carbonated concrete blocks that were subjected to different gas flow configurations are shown in Figure S7. The reference concrete block was modeled using an equivalent Young's modulus of 14 GPa[6] for all block's sections.

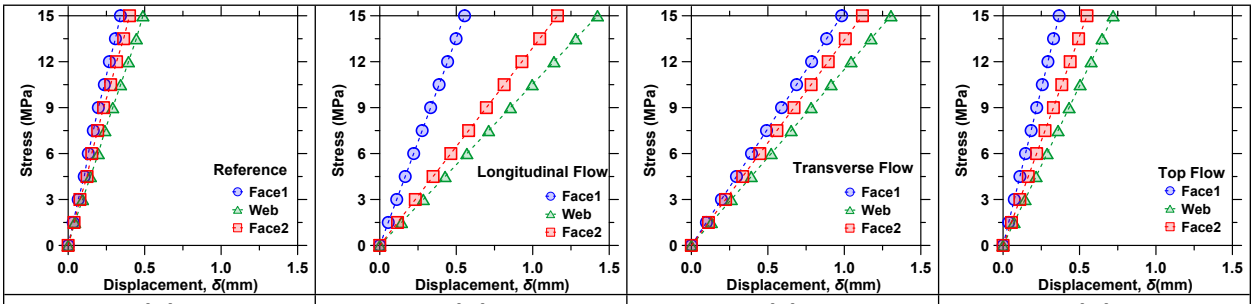

Figure S7: FEM simulations of uniaxial compressive stress-displacement responses for different sections of: **(a)** reference block, and for **(b)** longitudinal flow, **(c)** transverse flow, and **(d)** top flow configurations.

REFERENCES

1 D. C. Montgomery, *Design and analysis of experiments*, John wiley & sons, 2017.
2 D. C. Wilcox, *Turbulence modeling for CFD*, DCW industries La Canada, CA, 1998, vol. 2.
3 Y. Chen, F. Arbeiter and G. Schlindwein, *Numer. Heat Transf. Part Appl.*, 2012, **61**, 38–60.
4 C. Multiphysics and C. Module, *Version COMSOL Multiphysics*.
5 K. D. Hjelmstad, *Fundamentals of structural mechanics*, Springer Science & Business Media, 2007.
6 M. S. J. Committee, *Mason. Soc. Boulder CO*.